

Optimal Design of the Bearingless Induction Motor

Jiahao Chen*, Member, IEEE, Yusuke Fujii*, Member, IEEE, Martin W. Johnson†,

Ashad Farhan*, Student Member, IEEE, Eric L. Severson* Member, IEEE

*Department of Electrical and Computer Engineering, University of Wisconsin-Madison, Madison, WI 53706 USA

†Department of Mechanical Engineering, University of Wisconsin-Madison, Madison, WI 53706 USA

Abstract—The bearingless version of the induction motor (IM) has unacceptable performance for high speed or significant power applications. This is due to design challenges that are unique to the bearingless IM, including fundamental topology differences, rotor current induced by the suspension field, and a lack of techniques that can rapidly and accurately model the machine. This paper presents a complete investigation into the design topology, modeling, and optimization of bearingless IMs to identify high-efficiency, power-dense designs for a high speed industrial compressor system. Key differences in the design of the bearingless IM from that of the classical line-fed IM are explored and an analytic design approach is proposed. A pole-specific rotor and a combined stator winding are used to improve the machine performance. Computationally-efficient finite element modeling techniques are proposed and evaluated based on their ability to accurately calculate bearingless IM design performance metrics. An optimization framework is developed around these advancements using the multi-objective evolutionary algorithm based on decomposition (MOEA/D). The paper exercises this framework to explore the design space of four different slot-pole combination bearingless IMs for a 50 kW, 30,000 r/min compressor. High performance designs are identified that achieve > 96% efficiency with a torque density competitive with high performance servo motors that use contact bearings.

Index Terms—Bearingless motor, induction motor, magnetic suspension, finite element analysis, optimization.

I. INTRODUCTION

Bearingless motors are electric motors that are capable of producing torque and lateral forces on their shaft. They operate as both a motor and active magnetic bearing (AMB), but without the AMB hardware—offering all the benefits of magnetic levitation while reducing the system cost and complexity associated with AMBs. During the last two decades, interest in this technology has been rapidly growing and has led to the development of bearingless versions of nearly all types of electric motors [1], [2]. Induction motors (IMs) are regarded as the “workhorse” of industry due to their robust structure, suitability for harsh environments, low cost components, and extreme reliability. They are also becoming increasingly popular for high speed designs [3]–[5]. The design of bearingless versions of IMs has received only limited research attention, i.e. [6]–[8]. Current literature on the bearingless IM primarily focuses on control [9]–[14] or sensing [15]–[18].

To the authors’ knowledge, this will be the first paper to present a detailed investigation into the modeling and optimal design of the bearingless IM. The paper targets an application space of high-speed industrial compressors of significant

The authors would like to acknowledge the support of the Wisconsin Electric Machines and Power Electronics Consortium (WEMPEC).

power levels. The potential impact, design requirements, and configurations for bearingless motors in this space has been reviewed in [2]. This paper considers a bearingless IM that provides 2 degrees-of-freedom (DOF) for shaft suspension, with AMBs used to support the remaining DOF, (see Fig. 2a).

The design of the bearingless version of the IM is inherently more complex and challenging for the following reasons:

- 1) The magnetic suspension field used for levitation rotates at a different speed than the torque producing field, and thereby potentially induces large currents into the rotor that can degrade the machine efficiency, suspension force capability, and result in thermal challenges [1], [7], [19].
- 2) Suspension force ripple (the dual of torque ripple) can lead to instability in the suspension regulator [1]. Highly accurate machine models must be used in the design process to avoid designs that have stability challenges.
- 3) Accurate models of the bearingless IM based on conventional finite element analysis (FEA) techniques are too computationally-expensive for use in design optimization; this is because the induced rotor currents are a transient effect that develop over several electrical periods.
- 4) The design objectives (high efficiency and torque density and low force ripple) are in trade-off and sensitive to several geometric parameters.

The combination of these items make the bearingless IM exceedingly difficult to design. This paper systematically investigates and proposes solutions to these challenges.

The primary goal of this paper is to create the science necessary to develop bearingless IM technology as a high performance solution for industrial compressors. The paper first reviews literature on fundamental bearingless IM design considerations in Section II. From this review, the DPNV combined stator winding and pole-specific cage rotor are identified as providing the greatest potential for yielding a high performance motor design. Section III proposes an analytic method to dimension this topology of bearingless IM by modifying the classical IM design approach. This new dimensioning method is based on the design’s torque specification, but not the magnetic suspension specification (due to analytic model inaccuracies of suspension force ripple). The design produced by Section III is intended to be an initial design that is improved through an optimization process using accurate FEA models. However, as already mentioned, the direct use of transient FEA comes with prohibitively long solve times. Section IV proposes several FEA modeling strategies to significantly reduce the computation time required

to evaluate the performance of a bearingless IM design and identifies a technique suitable for use in design optimization. Section V experimentally validates the accuracy of the selected computationally-efficient FEA modeling technique through test results from a prototype bearingless IM.

Section VI compiles these advancements (the topology selection, dimensioning procedure, and computationally-efficient FEA model) into an optimization framework which is developed specifically for the unique requirements of optimizing a bearingless IM. This involves identifying the breakdown slip of each design candidate and defining appropriate objectives and constraints to obtain high performance in both motor and suspension operation. Finally, this optimization framework is used in Section VII to explore the design space of four different slot-pole combination bearingless IM machines and draw conclusions about this technology's performance potential in this application space (30,000 r/min, 50 kW industrial compressor). A particularly promising design is investigated in more detail and shown to have an efficiency of 96.9% and a torque density in the range of high performance servo motors.

Conference versions of this paper were published as [20], which explored computationally efficient modeling techniques, and [21], which developed the optimization framework. The present paper expands on these prior publications to provide experimental validation of the modeling techniques and a more detailed investigation into the bearingless IM design space.

II. BEARINGLESS IM DESIGN CONSIDERATIONS

The design of high speed IMs and bearingless IMs share common considerations from the aspect of high speed operation. To avoid excessive iron loss, a large air gap length is usually adopted [3], [22] and rotor loss can be reduced by using magnetic wedges or adding notches to the stator teeth [23]. There are, however, three primary design differences for bearingless IMs which can be summarized as follows:

- 1) Bearing design; high speed IMs use contact bearings [24] or AMBs [4], [25], [26]; bearingless IMs integrate the functionality of an AMB into the motor, making bearing design an integral part of the magnetic design process.
- 2) Stator winding design; the bearingless motor requires that the stator winding create a second magnetic field in the airgap to produce suspension forces.
- 3) Rotor design; high speed IMs use solid or cage rotors [4], [5]; these rotors degrade bearingless IM performance.

This section now reviews implications of design aspects 2) and 3) and topology choices that exist within the literature.

A. Stator Winding Design

Bearingless IMs require the stator winding to create two magnetic fields in the airgap, a p pole-pair field for torque (this is standard to all ac machines) and a $p_s = p \pm 1$ pole-pair field for suspension forces (this is unique to bearingless machines). Winding arrangements that are able to generate these two magnetic fields have been developed in the literature and can be classified as either a "separated" winding [1] or a "combined" winding. Combined windings are a more recent advancement and can be further divided into multi-phase (≥ 5

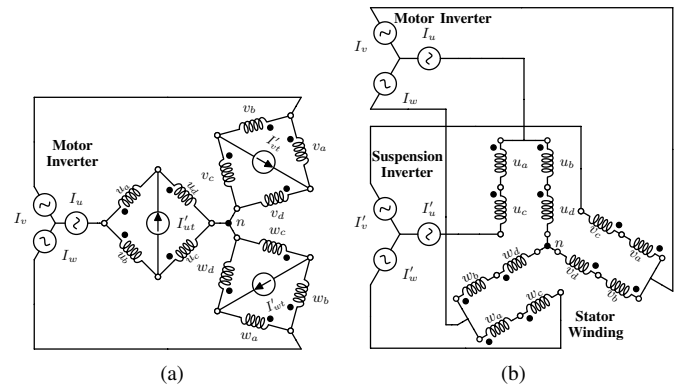


Fig. 1. (a) Bridge and (b) Parallel configurations of the DPNV winding [27].

TABLE I
FORCE ATTENUATION IN EXAMPLE $p = 2$, $p_s = 1$ IM WITH CAGE ROTOR

Rotor speed	0	1275	14775	[rpm]
Electrical frequency	7.5	50	500	[Hz]
Motor field rotor slip freq.*	7.5	7.5	7.5	[Hz]
Suspension field rotor slip freq. [†]	7.5	28.75	253.75	[Hz]
Suspension force	125	42	8	[N]

*Motor field slip freq. = $p \times (\text{motor field speed}^{\ddagger} - \text{rotor speed})$.

[†]Susp. field slip freq. = $p_s \times (\text{susp. field speed}^{\ddagger} - \text{rotor speed})$.

[‡]Field speed [s^{-1}] = electrical frequency / pole pair number.

phases) windings [17], [28]–[31] and DPNV (Dual Purpose No Voltage) windings [27], [32]–[35].

Separated windings use two distinct stator windings: one winding for creating the p pole-pair field (torque winding) and a second winding for creating the p_s pole-pair field (suspension winding) [1]. This results in the stator slot space being permanently allocated based on a fixed turns ratio between the torque and suspension windings. Since the suspension winding must be oversized to handle emergency conditions, this winding approach significantly reduces the slot area available for the torque producing winding compared to a standard IM—and thereby reduces the motor's torque density [2].

The combined winding can dynamically allocate the slot space between suspension and torque current because it uses the same coils to produce force and torque. Previous studies [2], [19], [36] have shown that with careful machine design, combined windings can increase the machine torque density and efficiency to levels near that of non-bearingless motors. However, combined windings typically require more power electronic drive components or higher Volt-Ampere rating devices than separated windings [37].

The bearingless IMs designed in this paper utilize DPNV windings. The distinguishing features of the DPNV winding are that the suspension current path has no back electromotive force (EMF) and standard motor drives can be utilized for torque creation. DPNV windings can be connected as bridge [32], [33] or parallel configurations [27], [34] shown in Fig. 1. A detailed FEA modeling study of a bearingless squirrel cage IM with a bridge DPNV winding is reported in [38]. Power electronic drive implementations are detailed in [34], [37].

B. Rotor Design

The bearingless IM poses a challenging paradox for the rotor design—while the torque field must induce currents in the

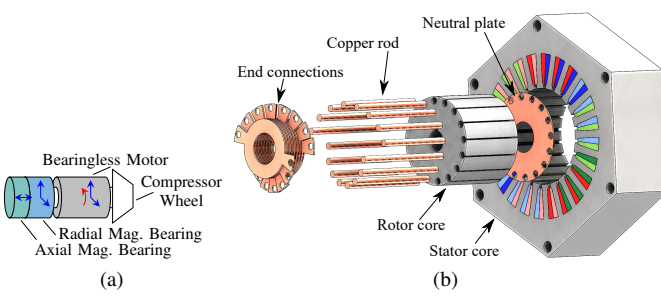


Fig. 2. Proposed bearingless IM (a) system [41] and (b) machine topology.

TABLE II
SPECIFICATIONS AND CONSTRAINTS SUMMARY

Specifications	50 kW, 30,000 r/min (torque = 15.9 Nm)
Reference Performance	$\eta > 95\%$, $E_a < 6$ deg
Mechanical Constraints	Tip speed = 150 m/s (rotor radius = 47.75 mm)
Thermal Management Strategy	Forced air cooling with current density limits: $J_s = 4$ Arms/mm ² , $J_r < 8$ Arms/mm ² , and drop shape rotor slot

rotor to create torque, any currents induced by the suspension field will negatively impact the machine's performance.

Consider an example of producing a constant direction force vector (i.e., to support the rotor's weight). This requires a suspension field in the air gap which rotates at a different speed than the torque producing field [1]. This means that the rotor has an additional slip speed, relative to the suspension field. In a cage rotor design, rotor currents induced by the suspension field cause undesired torque, losses, and attenuation and delay in the suspension forces. While suspension performance issues can be overcome through advanced control techniques, i.e. [19], [39], the additional rotor currents may result in thermal issues and low efficiency [1], [19]. Table I summarizes a case study of a cage rotor bearingless IM considered in the conference version of this paper [20] through transient FEA at different rotational speeds. Here, the suspension force amplitude decreases from 125 N (no rotation) to 8 N (high speed rotation) for the same magnitude of stator currents. This demonstrates that low speed bearingless IMs may be able to utilize a cage rotor (see e.g., [40]), but that challenges become more significant in high speed machines.

For the purpose of suspension operation, it is preferable to have no rotor bars, and therefore no currents induced in the rotor by the suspension fields [42]. Two solutions that allow for induced rotor currents from the torque field but not the suspension field include the pole-specific cage rotor [6], [7], [43], [44] and a wound rotor [45], [46] designed to not link the suspension field. In this paper, the pole-specific cage rotor approach is adopted. While this approach eliminates interference from the suspension fields, it poses new design challenges due to the requirement of multi-layer end connections, shown in Fig. 2b. This makes the rotor more difficult to manufacture and increases its axial length [6]. For example, a $Q_r = 32$, $p = 2$ rotor requires 8 layers of end connections.

III. BEARINGLESS IM ANALYTIC DESIGN

This section proposes a procedure to design a bearingless IM for a high speed compressor application based on the

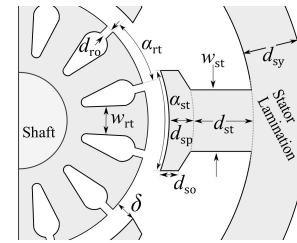


Fig. 3. Parameterization of bearingless IM geometry.

design considerations outlined in Section II. The system configuration of the compressor is shown in Fig. 2a and the motor topology with a pole-specific rotor is shown in Fig. 2b. The proposed design procedure follows analytic equations governing the motor performance and does not guide the design based on the suspension performance. It is intended to produce a set of approximate dimensions for the cross-section depicted in Fig. 3 that can then be refined with an FEA-based design optimization in Section VI, where the suspension performance can be accurately modeled. The procedure consists of following the steps and design equations of [47, Ch. 7], but modified by the design decisions and specification of Table II as detailed in the following subsections. Section VI, uses this procedure to construct "initial" designs for the bearingless IMs that are optimized.

A. Stator Winding Design

This paper designs the stator winding as an air cooled DPNV winding using the following methodology.

1) *Coil Parameters:* The stator current density is fixed at $J_s = 4$ Arms/mm². The slot fill factor is assumed as 0.5.

2) *Pole-Pairs:* Selecting the motor and suspension pole combination is a trade-off between motor and suspension performance and subject to constraints of the DPNV winding (summarized in [27]). From the motor perspective, a low value for p (i.e. $p = 1$ or $p = 2$) is preferred to maximize the machine's power factor [47]. For inner-rotor motors, selecting $p_s = p + 1$ increases the suspension force capability because the Lorentz and Maxwell forces are in the same directions [2]. However, this may not always be possible. For example, one of the symmetry constraints of the DPNV winding is that the number of motor phases must be co-prime with the value of p_s . This means that a three phase DPNV winding cannot be created with $p = 2$ and $p_s = 3$.

3) *Winding Layout:* The winding is designed following the procedure published in [27]. Later sections of this paper optimize different bearingless IMs that make use of the following two stator windings:

- 1) $Q_s = 24$ stator slots, $p = 1$, and $p_s = 2$ pole-pairs and
- 2) $Q_s = 24$ stator slots, $p = 2$, and $p_s = 1$ pole-pairs.

The DPNV design steps for winding design 1 is illustrated via phasor diagrams in Fig. 4a–4c and the winding schematic is shown in Fig. 4d; the winding schematic for design 2 is presented in the conference version of this manuscript [21].

B. Rotor Design

This section provides the design methodology used to design the pole-specific rotor.

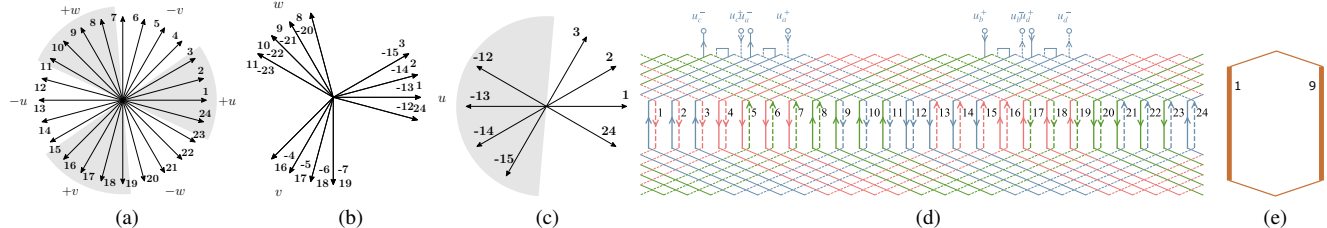


Fig. 4. Stator DPNV winding design diagrams for $Q_s = 24$, $p = 1$, $p_s = 2$ per [27]: (a) star of slots for torque winding layout; (b) torque connection star at torque frequency; (c) torque phase u connection star at suspension frequency to determine which coils to reverse for suspension winding; (d) resulting winding schematic—“+” terminals correspond to the dotted terminals in Fig. 1. (e) Rotor winding schematic; only one phase is shown.

1) *Rotor slot shape*: High speed IMs typically use either drop-shaped or round rotor slots. While round rotor bars can reduce stress on the lamination [48], this paper recommends the drop shape depicted in Fig. 3 to improve thermal performance. Section VII-A3 will show that the drop-shape can also lead to more efficient and torque dense bearingless designs.

2) *Rotor Outer Radius*: To maximize power density, high speed IM designs typically utilize the largest rotor radius value that results in a structurally stable rotor. The analytic design process accomplishes this by enforcing a maximum rotor tip speed (or surface speed) and then uses the corresponding rotor radius. High speed IM design examples in the literature (see [5], [47]) utilize laminated rotor tip speeds up to 200 m/s. This paper conservatively selects a tip speed of 150 m/s, corresponding to a rotor outer radius of 47.75 mm.

3) *Current Density*: The rotor bar current density is assumed to be $J_r = 6.5 \text{ Arms/mm}^2$ to utilize air cooling [47].

4) *Rotor Winding*: The pole-specific rotor of [6] is used. The number of rotor slots Q_r is selected by using guidelines in [47]. Four different rotors are considered in Section VI. The winding schematic is provided for the $p = 1$, $Q_r = 16$ rotor winding in Fig. 4e, which is equivalent to an 8 phase, full pitch winding. Since each phase consists of only two rotor bars, the end connections on one side of the rotor can be implemented with a single neutral plate as shown in Fig. 2b. The winding schematic for $p = 2$, $Q_r = 32$ is shown in [21, Fig. 2b], the conference version of this paper.

C. The Design Template for Optimization

The design produced by the analytic sizing steps of this section will be used as an “initial” design from which to start the optimization process. The later sections of this paper consider the 2D template design depicted in Fig. 3 that is defined by the optimization algorithm selecting the nine geometric variables listed in (1).

$$x = [\delta \ w_{st} \ w_{rt} \ \alpha_{st} \ \alpha_{rt} \ d_{so} \ d_{ro} \ d_{st} \ d_{sy}]^T \quad (1)$$

All other aspects of the geometry depicted in Fig. 3 are derived from these nine variables based on the provided design specifications of stator slot fill factor, current density (rotor and stator), and tip speed and by fixing $d_{sp} = 1.5d_{so}$. The axial length of the motor design is determined based on the length required to meet the power specification. Stator and rotor steel is modeled as 29-gauge (0.355 mm thick) M-19 steel.

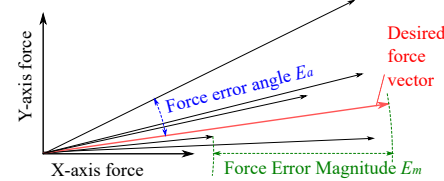


Fig. 5. Force vector error definitions; vectors calculated over one revolution.

IV. MOTOR PERFORMANCE EVALUATION METHODS

The goal of this section is to develop an accurate and computationally-efficient modeling technique for bearingless IMs that can be linked to a design optimization algorithm in Section VI. Typical global search algorithms used in electric machine design require the evaluation of hundreds of thousands of candidate designs. This means that the modeling technique must have low computational cost. IMs are notoriously complicated to model due to the startup transients associated with the induced rotor currents. The required computational effort is even greater for bearingless IMs due to the requirement of highly accurate force calculations.

This section evaluates the proposed bearingless IM models based on their ability to accurately calculate torque and suspension force performance metrics. In this analysis, torque ripple T_{rip} is defined as the peak-to-peak value of the torque profile over one rotor revolution. Suspension force ripple is quantified in terms of vector error as a worst case magnitude E_m and angle E_a error that occurs over one rotor revolution [49] when currents are flown so as to produce a constant force vector. An illustration is provided in Fig. 5 to clarify these definitions. Machines with a large force error angle can experience instability in the suspension position regulator [1]. Typical bearingless motor designs minimize force error angle to be within 5° [49], which places stringent requirements on the level of accuracy required of the modeling tool.

A. Candidate Bearingless IM Modeling Techniques

Several FEA-based modeling techniques are now proposed for the bearingless IM. All of these techniques assume that a desired slip frequency is predetermined. During a design optimization, this is the breakdown slip (the slip value that results in the maximum amount of torque [50, p.325]). For all analyses in this paper, the breakdown slip of a design is determined by using an eddy current FEA model to test the torque at different stator current excitation frequencies.

1) *Transient FEA*: A high fidelity transient FEA model with a small time-step size is the most accurate method to evaluate the performance of an IM design. Unfortunately, this

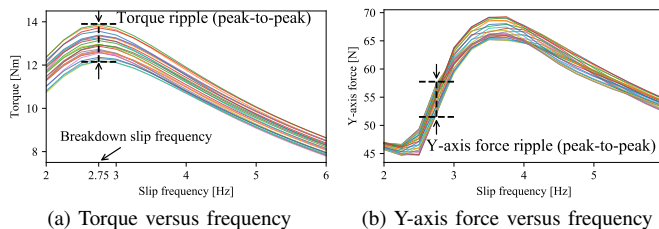


Fig. 6. Example eddy current FEA in small slip region at 24 rotor positions over a rotor slot pitch. Each trace corresponds to one rotor position.

approach has far too high of computational expense to be used in the optimization process (an accurate evaluation of a single candidate design requires several hours). There are several known methods to accelerate transient FEA modeling of an IM, including [51]–[53] and [54, Sec. 2.3]. For example, by using the solution of an eddy current solver to initialize the rotor currents of a transient FEA, the model rapidly reaches steady state conditions. However, even with these techniques, the solving time is still too long. This is especially true for a high frequency IM, because the maximum time-step size is severely limited by the high stator frequency, while the end-time must be long due to the low slip frequency.

This modeling technique (with rotor currents initialized by an eddy current solve) is treated as the baseline, against which all other techniques explored by this paper are compared.

2) *Eddy Current FEA at Multiple Rotor Angles*: In this technique, an eddy current solver is used where the stator is excited with currents at the slip frequency. The model is solved for different rotor positions θ to capture the slotting effect [55], which includes variation in amplitude of the fundamental component of rotor current and the variation in air gap permeance. Figure 6 illustrates how torque and force ripple can be extracted from the solution data. Each curve corresponds to a different rotor position θ . The peak-to-peak torque (or force) ripple is measured by evaluating the maximum deviation in torque (or force) at the breakdown slip frequency between all of the curves (values of θ).

3) *Static FEA with Predetermined Rotor Currents*: This technique uses static FEA by assigning rotor bar currents as a function of rotor position. The rotor currents are extracted from an eddy current solver for a single rotor position θ as complex numbers $\hat{I}_n \in \mathbb{C}$:

$$\hat{I}_n = \hat{I}_n e^{j\phi_n}, \quad n = 1, 2, 3, \dots, Q_r, \quad j^2 = -1 \quad (2)$$

which indicate the magnitude \hat{I}_n and phase angle ϕ_n of each bar's current at the slip frequency as a function of time. For constant rotor speed Ω , time t is related to the rotor position θ as $t = \theta/\Omega$. Rotor current $I_n(\theta)$ is determined for bar n as

$$I_n(\theta) = \hat{I}_n \cos(\omega_{\text{slip}}\theta/\Omega + \phi_n) \quad (3)$$

where the slip angular speed is $\omega_{\text{slip}} = \omega_s - p\Omega$ and ω_s is the synchronous angular speed. The performance metrics are calculated as a function of θ by evaluating the static FEA model at different θ values.

4) *Transient FEA with Two Time Step Sections (T2TS)*: This technique modifies the transient FEA approach of Section IV-A1 by utilizing different time step sizes. Initially, the

TABLE III
NUMERICAL RESULTS OF THE FEA MODELS FROM FIG. 7

FEA model	Average torque [Nm]	Torque ripple [%]	Average force [N]	E_m [%]	E_a [deg]
Ref. Transient FEA	14.7	1.1	144.7	3.6	2.2
T2TS FEA	13.5	1.3	146.8	4.0	2.1
Eddy Current FEA	14.9	0.8	163.9	1.2	0.3
Static FEA	14.5	0.9	139.5	5.1	3.4

simulation uses a relatively large time step size. This first time section lasts for half of the slip period and allows the rotor currents to reach steady state within a small number of time steps. In the second time section, a small time step size is used (similar size to the value of Section IV-A1) to accurately evaluate the design performance metrics. This second time interval lasts for half of the stator period. The number of time steps in either section can be adjusted to trade-off the computational-cost and accuracy. This paper uses 24 time steps in the first interval and 32 steps in the second interval.

B. Accuracy Comparison of Motor Modeling Techniques

The bearingless IM modeling techniques are now exercised to explore their accuracy on different machine designs. Each investigated modeling technique is compared against the reference transient modeling technique described in Section IV-A1. Comparison quantities are given as either:

- i) an absolute difference, for example “force error angle difference [deg]” is calculated as $E_a^{\text{Static}} - E_a^{\text{Ref.Tran.}}$, or
- ii) a normalized difference, indicated by specifying the difference as per unit “p.u.”; for example “force magnitude difference [p.u.]” is calculated as $\frac{|F|^{\text{Static}} - |F|^{\text{Ref.Tran.}}}{|F|^{\text{Ref.Tran.}}}$.

The models are evaluated at the breakdown slip and under rated coil current. The circuit of Fig. 1b is used to provide stator currents, where 97.5% of the rated coil current is allocated to produce torque and 2.5% of the rated current is allocated to produce forces. This requires that both suspension and torque currents be excited at the same electrical frequency (500 Hz). The following types of analysis are performed:

1) *Model Comparison for a Single Example Design*: The design procedure of Section III was used to create an initial design for a bearingless IM with $p = 2$, $Q_r = 36$, $Q_s = 24$. The FEA techniques developed in Section IV were used to calculate this design’s torque and force waveforms, shown in Fig. 7 to illustrate these techniques. Force and torque performance metrics are extracted from these waveforms and listed in Table III. The eddy current FEA (obtained over one rotor slot pitch–10 mech. deg) and the static FEA results (obtained over 90 mech. deg rotor rotation) are temporally extended for comparison purposes in Fig. 7. Both transient solutions are initialized via an eddy current solution of the rotor bar currents, which nearly eliminates the start up transient in Fig. 7. The first portion of the T2TS corresponds to a coarse time step (as described in Section IV-A4), and the suddenly thick trace toward the simulation end time corresponds to when the fine time-step is used for performance metric calculations.

2) *Model Comparison for 50 Random Designs*: The FEA models were used to evaluate fifty bearingless IM designs

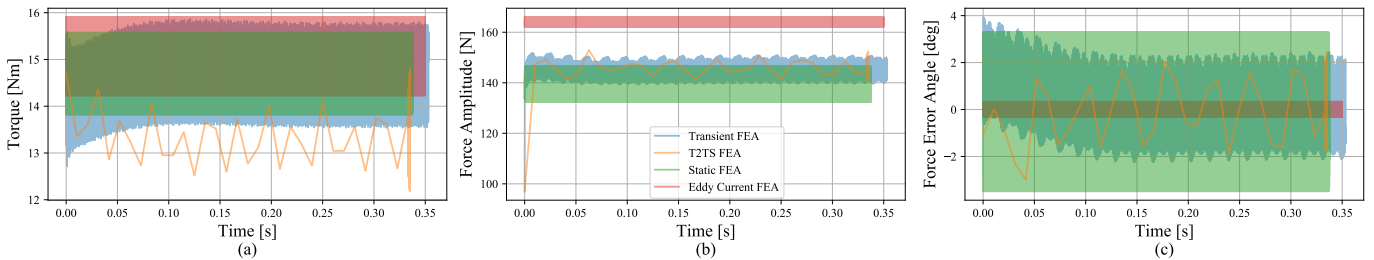


Fig. 7. FEA calculations of the motor modeling techniques at 30,000 r/min from Section IV for an example bearingless IM design: (a) torque; (b) force amplitude; (c) force error angle. Force and torque results of eddy current FEA and static FEA are temporally extended for comparison with transient FEA.

TABLE IV
STATISTICAL DATA OF THE 50 RANDOM DESIGNS FROM FIG. 8.

FEA model w/ regular step size	Torque diff. [p.u.]	Torque ripple diff. [%]	Force mag. diff. [p.u.]	Force err. mag. diff. [%]	Force err. angle diff. [deg]
T2TS FEA	-0.042 (1.0×10^{-4})*	4.8 (24)	0.007 (0.001)	-1.0 (4.2)	-0.5 (1.3)
Eddy Current FEA	0.023 (5.1×10^{-4})	-6.4 (50)	0.090 (0.035)	-10.0 (150)	-6.1 (75.0)
Static FEA	-0.008 (2.4×10^{-4})	-1.7 (22)	-0.010 (0.004)	6.1 (39)	4.9 (51.0)

*Note: all statistical data are in the format of “mean (variance)”. The FEA model is better if its data are closer to 0.

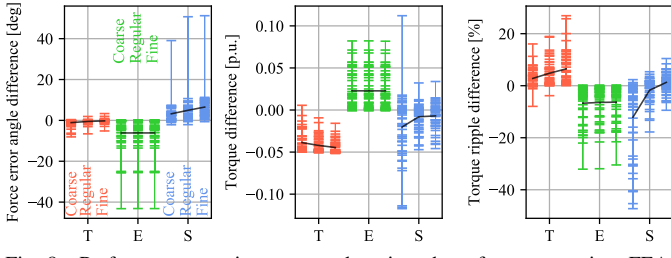


Fig. 8. Performance metrics compared against the reference transient FEA; label T—“T2TS”; E—“Eddy current FEA”, and S—“Static FEA”. Individual designs are indicated with a dash line. Black lines connect the mean value across different solving steps. For T2TS, the solving steps for the second interval are 16, 32 and 400; eddy current FEA, the steps for one rotor slot pitch are 12, 24, 48; static FEA, the steps for 90 mech. deg are 18, 45, 180.

that were generated by creating a random x (1) and using the example design of Section IV-B2 as a template. The results are shown in Fig. 8 with their statistical data listed in Table IV. The accuracy of the performance metric calculations is determined by comparing the values calculated by the three computationally-efficient modeling methods to the reference transient FEA. Sensitivity of each technique to the solution’s rotor position step size is indicated in Fig. 8 as three solution sets corresponding to a coarse, regular, and fine step size. For a transient solution, the rotor step size corresponds directly to the time-step size. For the static and eddy current modeling techniques, this corresponds to the increment size used for rotor position θ . The average time to evaluate a single candidate design for the proposed T2TS FEA, the eddy current FEA, and the static FEA (with a regular solving step) are 58s, 40s, and 33s on a workstation PC with an Intel i7-7820X. Note that the typical solving time needed for reference transient FEA is in excess of 4 hours.

C. Selection of Modelling Approach for Design Optimization

The analysis results from Section IV-B are now compiled to determine which techniques are most suitable to use in a design optimization. Based on the following discussion, the T2TS approach has been selected for the optimization framework presented in Section VI.

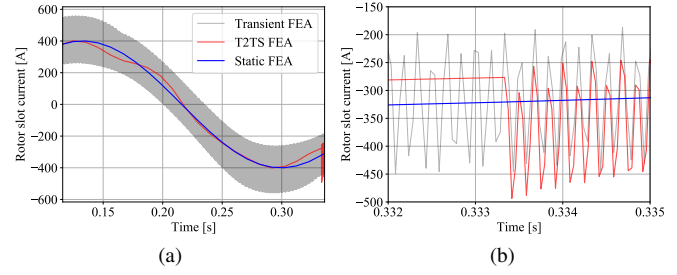


Fig. 9. Rotor current calculations of the FEA models zoomed (a) out; (b) in.

1) *Eddy Current FEA at Multiple Rotor Angles:* The eddy current solver yields inaccurate force and torque ripple calculations. Refinement of the step size does not appear to increase the model accuracy, and Table III indicates that this modeling approach cannot be reasonably expected to accurately determine whether a design is within the 5° error angle calculation requirement mentioned earlier. A potential cause for the inaccuracies of the eddy current solution (and area for potential future improvement) may be how the eddy current solver accounts for magnetic saturation [56].

2) *Static FEA with Predetermined Rotor Currents:* Static FEA is shown to be accurate for calculating the torque performance. However, this method is prone to inaccurate force ripple calculations, which are not improved through the use of a finer step size. The force ripple inaccuracies are likely due to the assumption of sinusoidal rotor slot currents inherent to this approach—see (3). Figure 9 presents the rotor bar currents of an example design, where the baseline transient FEA model calculates significant current ripple.

3) *Transient FEA with Two Time Step Sections:* According to Table III and IV, this approach is able to accurately calculate both the force and torque performance, and the accuracy is statistically improved through refining solving step (Fig. 8). When considering the critical error angle E_a metric, this approach (with “regular” step size) calculates E_a within $[-3.1, 2.0]$ deg for 49 out of 50 designs, while for the last design the E_a difference is -6.6 deg. It is concluded that this approach provides the most robust and computationally efficient models for bearingless IM design optimization.

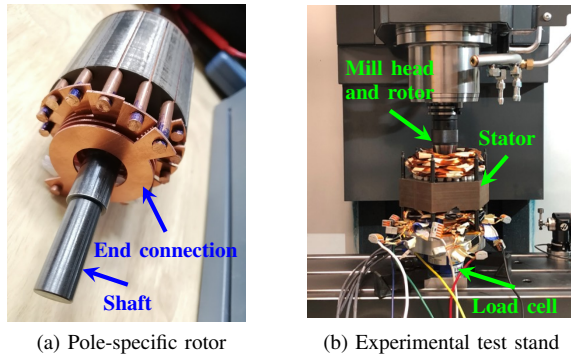


Fig. 10. (a) $p = 1$ pole-specific rotor; (b) CNC mill configured for use as a bearingless motor test stand.

V. HARDWARE PROTOTYPE

A bearingless IM prototype was built with a pole-specific rotor to validate the modeling framework of Section IV. The prototype was designed for rated speed (30,000 r/min) but fabricated with reduced stator outer diameter, rotor radius, and stack length compared to what is required for a 50 kW machine. These changes were made to make the prototype practical to manufacture and test with available resources. The prototype's winding schematic and a 3D CAD rendering were previously shown in Fig. 4 and 2b. Design information is summarized in Table V, where "max." torque and suspension current refer to the maximum current that can enter either the torque or suspension terminals of Fig. 1b while still remaining within the coil current rating. A CNC mill has been configured as a contact-free dynamometer to characterize the prototype, shown in Fig. 10b. The rotor is secured in the mill chuck and the stator is mounted to the x - y table through a 6 axis load cell. The load cell [57] measures reaction forces and torque on the stator, allowing for a comparison between FEA models and hardware at various operating points.

The bearingless IM models are validated in two ways. First, the models developed in Section IV are used to evaluate the torque and force performance metrics of the design as would be done in the optimization process. Emphasis is placed on validating the T2TS method (see Section IV-A4), as this is selected for use in the design optimization. Second, detailed (computationally-expensive) FEA models are used to model the prototype as accurately as possible. This validates that reasonable material parameters are used and that the prototype behaves as expected. The results are summarized in Table VI and VII, which are described in the following subsections.

The detailed FEA models include a measured rotor end ring resistance ($R_c = 0.116 \text{ m}\Omega$, described in Section V-A). The computationally-efficient models neglect this resistance because implementing it requires knowledge of the rotor's axial length, which is not known in the optimization process until after the computationally-efficient models have been evaluated. This is because the machine's axial length is determined based on the torque per axial length (calculated by the FEA model) in order to meet the power specification. Since the prototype's axial length is reduced, the end ring resistance and 3D field effects that are neglected in the 2D models have a more significant impact when evaluating the prototype machine than when used in the design optimization of Section VII.

TABLE V
PROTOTYPE DESIGN PARAMETERS

Number of torque p , suspension p_s pole-pairs	1, 2	-
Number of stator Q_s , rotor Q_r slots	24, 16	-
Turns per coil	16	-
Max. torque, sus. terminal current	13, 6.5	Arms
Breakdown slip frequency	12.5	Hz
Stator diameter, rotor radius, axial length	150, 31.8, 50	mm
Air gap length	2.65	mm

TABLE VI
EXPERIMENTAL VALIDATION OF MODELS

	Rated Torque [Nm]	Rated Force [N]
Prototype	1.15	5.6
Detailed FEA Model	1.14	4.9
T2TS Model	1.04	5.0

Differences between the detailed and computationally-efficient model calculations can be viewed as an estimate of the upper bound of uncertainty in the performance metric estimates.

A. Rotor Loss Measurement

The pole-specific rotor combined with the DPNV stator winding enables measurement of the rotor loss and effective rotor resistance at different slip frequencies. This is done by conducting a blocked rotor test and recording input power and rotor bar current (using a Rogowski coil). When rated AC currents are applied to the motor terminals and the suspension terminals are short-circuited (see Fig. 1b), current is induced in the rotor bars and the primary loss components are the stator and rotor winding losses (iron losses are negligible because of the low frequency). When rated AC currents are applied to the suspension terminals (and the motor terminals are open-circuited), no current is induced in the pole-specific rotor and the only notable loss component is the stator winding losses. The rotor loss is determined as the difference in measured input power between the two tests.

The measured rotor bar current is shown in Fig. 11a, where the computationally-efficient 2D FEA model (eddy current) is revealed to be particularly accurate. The rotor loss measurement results are shown in Fig. 11b, which reveals 0W of rotor loss at 0 Hz (as expected) and a notable difference in losses between the 2D FEA and the experiment at 60 Hz (49 W). This discrepancy is due to losses occurring in the rotor end ring (which are not modeled in the computationally-efficient FEA). An effective rotor end ring resistance of $R_c = 0.116 \text{ m}\Omega$ is found to minimize the least square error in the rotor loss data (see Fig. 11b) and is shown in the remainder of this section to also yield particularly accurate torque and AC force FEA results. While the computationally-efficient FEA will not capture the rotor losses in the end ring, these losses are insignificant at rated slip (12 W) relative to the power rating and neglecting them will not impact the machine optimization.

B. Torque Validation

Design performance metric results are presented in Table VI. These results indicate that the T2TS result underestimates the rated torque by approximately 10%. An underestimation of motor torque is expected based on Section IV-B

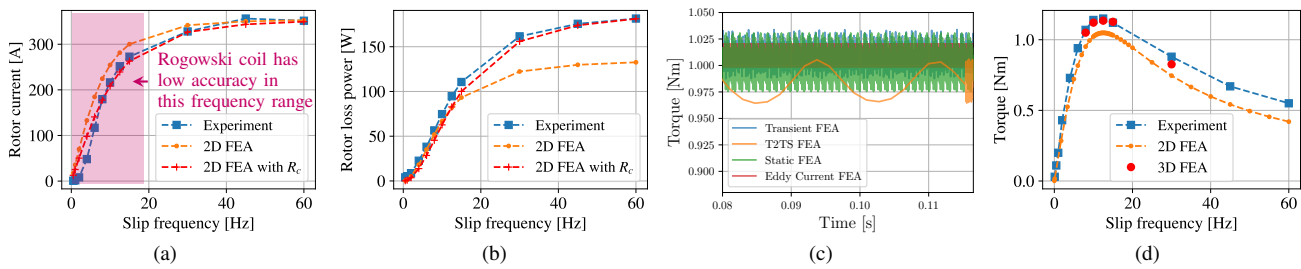


Fig. 11. Motor validation of the prototype; (a) rotor bar current-slip curve for rated current with blocked rotor; (b) rotor loss-slip curve for rated current with blocked rotor; (c) computationally-efficient model torque calculations; (d) torque-slip curve for rated current with blocked rotor.

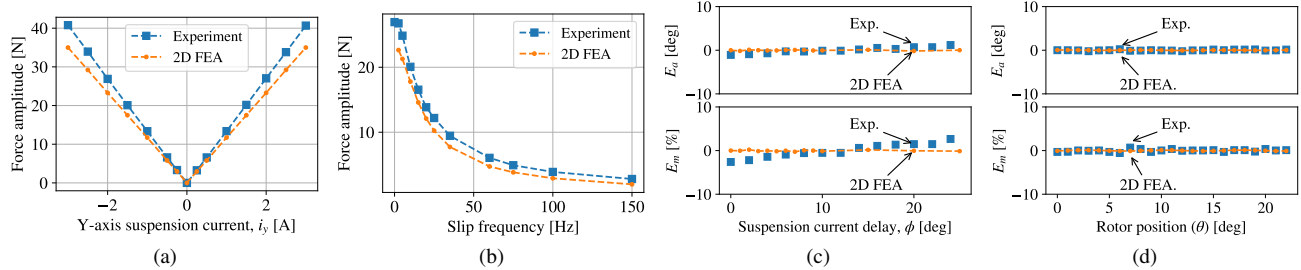


Fig. 12. Suspension force validation of the prototype; (a) static force capability; (b) force capability at different slip frequencies with a blocked rotor; (c) force error angle and magnitude as a function of rotor flux angle ϕ when $\theta = 0$ and (d) rotor position θ when $\phi = 0$.

TABLE VII
EXPERIMENTAL VALIDATION OF FORCE VECTOR ERROR

	E_m [%]	E_a [deg]
Prototype test: variable rotor flux angle ϕ	2.7	1.2
Prototype test: variable rotor rotation θ	0.7	0.2
Detailed FEA Model	0.4	0.2
T2TS Model	0.5	0.2

and Table IV, where this modeling approach underestimates torque by an average of 4% compared to a reference 2D FEA solve. Surprisingly, Fig. 11c reveals that all of the 2D modeling methods underestimate the prototype's rated torque. It turns out that for the prototype's short axial length, there is a significant impact from fringing fluxes in the axial direction that require 3D FEA to fully capture. Fig. 11d shows that 2D FEA (eddy current solution) underestimates each torque point while a computationally-expensive 3D transient FEA (includes $R_c = 0.116 \text{ m}\Omega$, solve time of approximately 24 hours per point) is able to precisely model the torque-slip characteristic¹. This underestimation of the prototype torque is not viewed to be problematic for the optimization process, as the rotor length can easily be adjusted after the optimization is complete.

C. Suspension Force Validation

Force tests are conducted with the CNC mill locking the rotor at zero speed. Performance metrics calculated with the T2TS method are compared against these results in Table VI and VII, as discussed below. In these tests, the motor currents are specified following the convention in [58] by using current space vectors² at the torque terminals \vec{i}_t and force-producing

¹Note that in Fig. 11c, the coils carry 97.5% of the “Max. torque terminal current” and 2.5% of the “Max. sus. terminal current” (see Table V), while in Table VI and Fig. 11d, the coils carry 100% of the torque current rating.

²Amplitude invariant space vector transformations are used.

components \vec{i}_s as defined in (4), where ϕ is the direct axis location (typically aligned with the rotor flux).

$$\begin{aligned} \vec{i}_t &= (i_d + j i_q) e^{j\phi} \\ \vec{i}_s &= (i_x + j i_y) e^{-j\phi} \end{aligned} \quad (4)$$

First, DC currents are used to measure the machine's force capability in Fig. 12a, where $i_d = 14 \text{ A}$, $\phi = 0$, and i_y varies. The small error between the prototype data and the FEA models is within the accuracy of the 6 axis load cell [57]. Next, an AC force test is performed to validate the force capability of the motor at different slip values and that the pole-specific rotor winding is functioning as expected. Sinusoidal suspension ($i_y = 2 \text{ A}$) and torque ($i_d = 14 \text{ A}$) currents are applied to the stator at the slip frequency (by increasing ϕ at this frequency) and the results are shown in Fig. 12b. The suspension force decreases as the motor slip frequency increases because increasing rotor currents (due to the torque field) attenuate the magnetizing airgap field. Interestingly, this plot indicates that operating the motor at low slip values can significantly increase the force capability.

The data from Fig. 12a and Fig. 12b is used to estimate the prototype's rated force in Table VI, which is defined as the force produced when coils are excited by 97.5% of the “Max. torque” current and 2.5% of the “Max. sus.” current (ac currents at the same electric frequency) with the rotor at the breakdown slip. The prototype force rating estimate is within 0.7 N of the FEA models, indicating a very close agreement.

Force vector error measurement results are reported in Fig. 12c and Fig. 12d with $i_y = 2 \text{ A}$ and $i_d = 14 \text{ A}$. In Fig. 12c, the direct-axis reference frame ϕ is rotated from 0° to 22.5° (corresponding to one rotor tooth/slot pitch) while the rotor is held stationary. In Fig. 12d, $\phi = 0$ and the mill rotates the rotor over one tooth/slot pitch. The results are summarized in Table VII and confirm that the prototype has exceedingly low force vector error. The test results are in

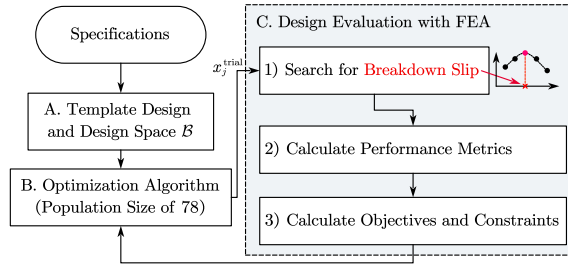


Fig. 13. Block diagram of the motor evaluation and optimization process.

excellent agreement with the FEA results; small discrepancies in Fig. 12c are attributed to a small amount of eccentricity that was observed when using the mill to center the rotor.

VI. BEARINGLESS IM OPTIMIZATION FRAMEWORK

The analytic design and computationally-efficient models developed in Sections III and IV are now combined with an optimization algorithm to create a framework to optimize bearingless IMs for high speed industrial compressor applications. The overarching framework is depicted in Fig. 13. Each box in this diagram is described in the following subsections.

A. Template Design and Design Space

At the start of the optimization, an initial design and a design template are created from the bearingless motor design specification following the procedure in Section III-C. Candidate motor designs are fully defined from this template when the optimization algorithm selects values for the vector x —see (1). The design space consists of all feasible x vectors and is restricted to reduce the optimization time by using the initial design ($x = x_{\text{ini}}$) to establish reasonable bounds on the geometric variables. Table VIII provides an example.

B. Optimization Algorithm

The multi-objective evolutionary algorithm based on decomposition (MOEA/D) [59] is used to search the design space. MOEA/D is reported to work well with large population sizes, compares favorably against other non-dominated sorting algorithms [59], and is intended for use in multi-objective optimization (MOO) with up to four objectives [60] making it a strong fit for the bearingless IM optimization requirements. Pareto non-dominated sorting of candidate designs is implemented based on Pareto dominance, where design x_A dominates another design x_B if all objective values of x_A are no worse than that of x_B and at least one of the objective values of x_A is better than that of x_B . During the comparison stage of non-dominated sorting, the j -th new-born trial design $x_{j,\text{trial}}$ will be discarded if $x_{j,\text{trial}}$ does not dominate the j -th design x_j from the population. This paper adopts the differential evolution variant of MOEA/D implemented by the software PAGMO [61]. A population size of 78 selected.

C. Design Evaluation

The shaded box in Fig. 13 is used by the optimization algorithm to calculate the optimization objectives of candidate

TABLE VIII
OPTIMIZATION OF p1Q_r32 DESIGN

Geometric Parameter	Symbol (x)	Bounds (\mathcal{B})	Initial (x_{ini})	Optimal (x_{optm})
Air gap length	δ [mm]	[1.3, 2.9]	1.44	2.06
Stator tooth width	w_{st} [mm]	[3.5, 10.4]	6.96	7.95
Rotor tooth width	w_{rt} [mm]	[4.9, 14.6]	9.73	5.10
Stator tooth tip span	α_{st} [deg]	[3.0, 12.0]	3.00	5.29
Rotor tooth tip span	α_{rt} [deg]	[0.6, 3.6]	2.25	2.44
Stator tooth tip depth	d_{so} [mm]	[0.5, 3.0]	1.00	2.49
Rotor tooth tip depth	d_{ro} [mm]	[0.5, 3.0]	1.00	1.19
Stator tooth depth	d_{st} [mm]	[21.5, 32.2]	26.84	32.12
Stator yoke depth	d_{sy} [mm]	[25.4, 38.1]	22.15	34.62

motor designs. Each design candidate is defined by x (1) along with the design template of step B. This is done in the following sub-steps (white sub-boxes in Fig. 13).

1) *Search for Breakdown Slip*: The breakdown slip frequency of the candidate design is determined by eddy current FEA. To expedite the searching process, five different slip frequencies are solved in parallel using FEMM [56].

2) *Calculate Performance Metrics*: Design performance metrics (torque, force, and losses) are calculated by using the proposed T2TS FEA method (see Section IV-A4) to evaluate the design at the breakdown slip frequency using JMAG Designer. The stator winding excitation is configured so that 97.5% of rated current is allocated for motor operation while the remaining 2.5% is allocated for suspension force. The suspension currents are excited at the motor's electrical frequency to produce a constant force vector (i.e., oppose gravity). Analytic equations are used to calculate copper loss (including end winding length) [62] and windage loss [49].

3) *Calculate Objectives and Constraints*: The following objective functions are minimized during the design process:

$$O_A(x) = -\text{TRV}, \quad O_B(x) = -\eta \\ O_C(x) = T_{\text{rip}}/(5\%) + E_m/(5\%) + E_a/(1 \text{ deg}) \quad (5)$$

These objectives are functions of performance metrics that are calculated during sub-step 2, where TRV [Nm/m³] is torque per rotor volume (which also is an indicator of the machine's active material cost), η [%] is efficiency, and T_{rip} [%], E_m [%], and E_a [deg] are defined in Section IV. Note that O_C is a weighted sum of ripple performance metrics. These metrics have been combined into a single objective function so that the optimization results can be readily visualized (with a 3D plot). To eliminate designs that have unacceptable ripple or suspension performance, four constraints are imposed as (6), where FRW [p.u.] is suspension force per rotor weight.

$$T_{\text{rip}} < 30\%, \quad E_m < 30\%, \quad E_a < 10 \text{ deg}, \quad \text{FRW} > 0.75 \quad (6)$$

VII. OPTIMIZATION RESULTS

The optimization framework developed in Section VI was used to explore the design space of the following slot-pole combinations of bearingless IMs:

- 1) $p = 1, p_s = 2, Q_r = 16, Q_s = 24$, labeled “p1Q_r16”,
- 2) $p = 1, p_s = 2, Q_r = 32, Q_s = 24$, labeled “p1Q_r32”,
- 3) $p = 2, p_s = 1, Q_r = 16, Q_s = 24$, labeled “p2Q_r16”,
- 4) $p = 2, p_s = 1, Q_r = 32, Q_s = 24$, labeled “p2Q_r32”.

All designs variants are optimized for the design specification of Table II and use 29-gauge (0.355 mm thick) M-19 steel and copper rotor bars. The stator winding schematic for designs

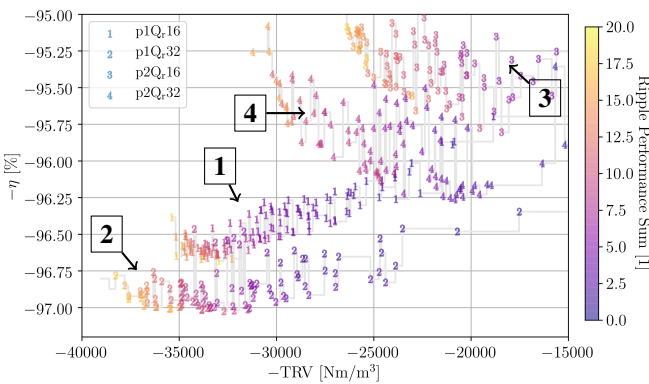


Fig. 14. Projection of 3D Pareto front onto the efficiency-TRV plane; O_C is indicated by the marker color. Only first rank Pareto front designs are shown.

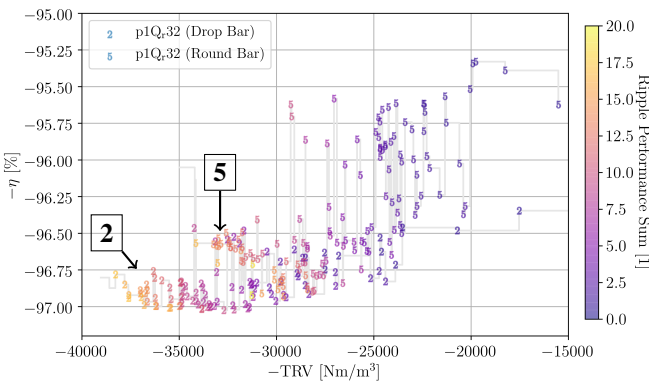


Fig. 15. Comparison of drop-shaped and round-shaped bar design.

1) and 2) is shown in Fig. 4 and the schematic for designs 3) and 4) is provided in the conference version of this paper [20]. This section examines trade-offs in the design space of each machine configuration based on the requirements of a high speed industrial compressor, where $\text{TRV} > 15 \text{kNm/m}^3$ and $\eta > 95\%$ is desired [2], and proposes a promising $p1Q_r,32$ design for a detailed analysis.

A. Pareto Front Comparison

This optimization utilizes three objectives (O_A , O_B , O_C) defined in (5), which means that the Pareto front is a surface in 3D space. The bearingless IM designs on the estimated Pareto front are projected onto the O_B - O_A plane ($-\eta$ vs. $-\text{TRV}$) in Fig. 14 (drop-shaped rotor bars) and Fig. 15 (round and drop-shaped rotor bars), where slot-pole combinations are indicated by markers “1”–“4”. Some designs have inferior TRV and efficiency but feature a lower O_C value (indicated by color) such that they are not dominated by others and are therefore still present on this plot. Designs with $O_C < 6$ are considered to have low ripple performance. These designs guarantee $E_a < 6$ deg to ensure suspension stability (see Section IV). The following observations can be made:

1) *Relationship Between Objectives:* Torque density TRV and efficiency η are *weakly* conflicting objectives, and they both *strongly* conflict with the ripple performance sum O_C . This is especially true for the $p = 1$ motor. TRV and η can be optimized at the same time if O_C is not a concern

TABLE IX
PERFORMANCE OF THE SELECTED OPTIMAL DESIGNS.

Metric / Name	$p1Q_r,16$	$p1Q_r,32$	$p2Q_r,16$	$p2Q_r,32$
TRV [kNm/m^3]	30.3	30.3	18.6	23.0
FRW [1]	1.44	1.81	2.01	2.84
$T_{\text{rip}} [\%]$	8.0	5.3	16.6	11.8
$E_m [\%]$	5.0	4.2	3.6	3.7
E_a [deg]	2.2	2.1	1.4	1.3
η [%]	96.33	96.92	95.45	95.76
Power factor [1]	0.786	0.804	0.650	0.656

(i.e., moving to the lower-left corner). On the contrary, O_C is improved towards the upper-right corner direction. In other words, by moving to the right in Fig. 14, O_C improves and TRV decreases with the same η , and by moving up in Fig. 14, O_C improves and η decreases with the same TRV.

2) *Comparison Between Slot-Pole Combinations:* In terms of TRV and efficiency, designs with $p = 1$ typically outperform designs with $p = 2$; designs with $Q_r = 32$ typically outperform designs with $Q_r = 16$.

3) *Comparison Between Rotor Slot Shapes:* Designs with round rotor bars have been optimized to compare the two rotor slot shapes introduced in Section III-B1. The results are shown in Fig. 15, where it is observed that the drop-shaped bar allows the design to reach higher TRV and higher efficiency η .

B. Selected Optimal Designs

For each combination of p and Q_r , the highest TRV optimal design with low ripple ($O_C < 6$) is selected for closer inspection. The performance metric calculations for these designs are summarized in Table IX, where the best value for each metric is indicated in bold. As previously observed, the two $p = 1$ designs are dominant in terms of torque performance (having higher TRV and η ; lower T_{rip} ; higher power factor). While these designs have not been optimized for FRW, a constraint (6) has been placed on the designs to ensure that they are able to support the rotor's weight with only 2.5% of rated current. Interestingly, the $p = 2$, $p_s = 1$ designs have the highest FRW values. This is a surprise, since Lorentz forces oppose Maxwell forces in $p = 1$ designs [2]. All designs meet the criteria for stable suspension operation ($E_a < 5$ deg) and the performance requirements for industrial compressors ($\text{TRV} > 15 \text{kNm/m}^3$ and $\eta > 95\%$).

A breakdown of the loss components for each of the optimal designs is shown in Fig. 16. Higher rotor copper loss, but lower iron loss is observed in the selected $p = 1$ bearingless IMs. The 2D cross-section of each of these designs is sketched in Fig. 17 with a uniform scale to facilitate comparison of the geometry. The figure shows the geometry variations one would expect based on the slot-pole combination (i.e., $p = 1$ designs have thicker yokes, $Q_r = 32$ designs have long, thin rotor teeth) [47]. There is significant variation in tooth tip shape, from open slots in Fig. 17a to semi-closed slots in Fig. 17d. Sensitivity to this variation is explored in Section VII-C1.

C. Detailed Analysis of the Optimal $p1Q_r,32$ Design

Figure 14 shows that the $p1Q_r,32$ design with drop-shaped rotor bars has the highest performance potential for high

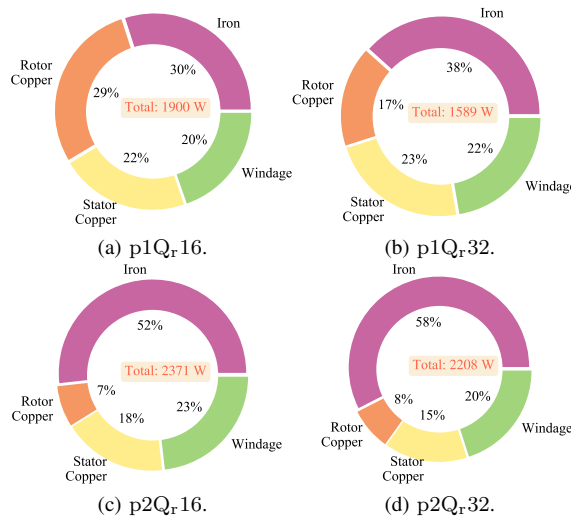


Fig. 16. Loss components of selected optimal designs.

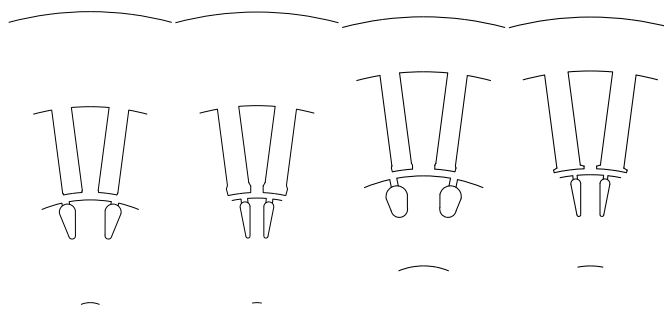


Fig. 17. Cross-sectional view of the selected optimal designs.

speed compressor applications. The dimensions of the optimal p1Q_r32 design from Table IX are provided in Table VIII. The design performance is now explored in more detail.

1) *Design Sensitivity to Slot Opening*: Fig. 18 presents the design sensitivity to α_{st} (see Fig. 3). The x axes of these plots is $\alpha_{st}/\alpha_{st}^*$, where α_{st}^* is the stator tooth tip span of an open slot (i.e., Fig. 17a). The torque density O_A , efficiency O_B and torque ripple T_{rip} can be remarkably improved by using larger α_{st} —this is expected, as semi-closed slots are frequently used in motor design. Interestingly, O_C , E_a , and E_m have a minimum around $\alpha_{st} = 0.7\alpha_{st}^*$ which corresponds to a slot where the tooth edges point inward. This shape of slot opening is unique to bearingless motors and is not observed in standard motor design. Finally, note that by tolerating greater values of E_m and E_a the motor performance can be improved considerably (i.e., using $\alpha_{st} = 1.3\alpha_{st}^*$ as opposed to $\alpha_{st} = 0.7\alpha_{st}^*$).

2) *Suspension Over Force Capability*: It is important for compressor systems to have substantial safety factor built into their force capability to handle emergency events, such as surge or an external disturbance. The over-force capability of the optimal p1Q_r32 design is investigated for two cases: 1) *Over current*—the torque current is maintained at 97.5% current rating, but the suspension current is increased so that the coil current rating is exceeded (this is acceptable for a short time interval); 2) *Rated current*—as the suspension current is increased, the torque current is decreased so that the coil current stays within its current rating. The results are

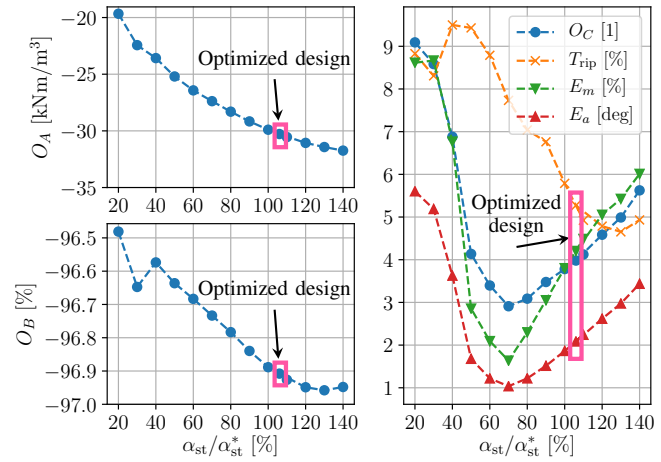


Fig. 18. Sensitivity analysis of optimal p1Q_r32 design with respect to α_{st} . α_{st}^* is the α_{st} value corresponding to a straight stator slot.

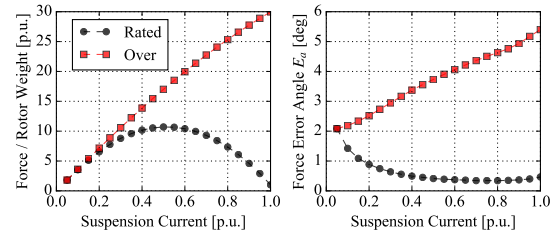


Fig. 19. Over-force capability of the selected p1Q_r32 design evaluated at the breakdown slip; base value of suspension current is the rated coil current.

depicted in Fig. 19. Case 1 shows an impressive transient force capability (30 times the rotor weight when the stator coils carry 2.0 p.u. current). Both cases are able to maintain an acceptable E_a value (suspension stability) over the entire range.

3) *Thermal Analysis*: A standard, low cost, thermal management system using a finned aluminum stator frame and forced axial airflow was designed for this machine based on losses extracted from the FEA models. By adding 3.4 m³/hr of 25° C axial airflow in the air gap, the temperature distribution is maintained well within material limits of the machine when operated at rated power (105° C on the stator and 108° C on the rotor). Introducing this axial airflow causes an additional 6 W of windage loss in the machine, which has a negligible impact on efficiency.

4) *Suitability for a High Speed Industrial Compressor*: The selected optimal p1Q_r32 design excels as both a motor and a suspension system. Only 1.4% of rated current is needed to support the rotor's weight and the design has an enormous over-force capability. This design clearly exceeds the motor design targets ($TRV > 15\text{kNm/m}^3$ and $\eta > 95\%$) set forth for a high performance industrial compressor in [2]. The fact that it does not require expensive permanent magnets and that it integrates magnetic bearing capability into the motor make it a compelling alternative to high speed motors that rely only on magnetic bearings. Additional development (beyond the scope of this paper) is needed to experimentally validate the optimized motor's performance at rated conditions as well as the pole-specific rotor's structural integrity and mass manufacturing feasibility.

VIII. CONCLUSION

This paper presents a comprehensive investigation into the development of high performance bearingless IMs. The paper makes several distinct contributions to the bearingless IM design and modeling process in an effort to create an optimization framework. The resulting framework is used to search the design space of high speed bearingless IMs and strong evidence is presented that the bearingless IM can be designed with efficiency in excess of 96% for a rated speed of 30,000 r/min and a rated power of 50 kW. This design performance makes the bearingless motor a compelling solution for high speed industrial compressors.

The paper reviews fundamental bearingless IM topology options to improve performance and proposes a topology based around a pole-specific cage rotor and DPNV combined winding. The paper then develops an analytic design sizing approach for this topology. One of the critical challenges encountered in optimizing bearingless IMs is the computation time associated with a direct implementation of transient FEA methods. This paper proposes and experimentally validates a computationally-efficient FEA-based modeling technique to rapidly calculate the performance metrics of a candidate bearingless motor design. Key performance metrics for bearingless IMs are identified and used to formulate objective functions and constraints that guide the design process towards high motor and suspension performance.

Optimization results reveal that bearingless IMs can provide the same motor performance as high performance IMs while gaining the substantial benefit of magnetic levitation. This strong electric performance warrants future work to develop the mechanical aspects of the pole-specific rotor design, namely structural integrity, thermal management, and mass manufacturing techniques.

REFERENCES

- [1] A. Chiba, T. Fukao, O. Ichikawa, M. Oshima, M. Takemoto, and D. G. Dorrell, *Magnetic bearings and bearingless drives*. Elsevier, 2005.
- [2] J. Chen, J. Zhu, and E. L. Severson, "Review of bearingless motor technology for significant power applications," *IEEE Transactions on Industry Applications*, vol. 56, no. 2, pp. 1377–1388, 2020.
- [3] A. Tenconi, S. Vaschetto, and A. Vigliani, "Electrical machines for high-speed applications: Design considerations and tradeoffs," *IEEE Transactions on Industrial Electronics*, vol. 61, no. 6, pp. 3022–3029, 2014.
- [4] R. Lateb, J. Enon, and L. Durantay, "High speed, high power electrical induction motor technologies for integrated compressors," in *Electrical Machines and Systems, 2009. ICEMS 2009. International Conference on*. IEEE, 2009, pp. 1–5.
- [5] D. Gerada, A. Mebareki, N. L. Brown, C. Gerada, A. Cavagnino, and A. Boglietti, "High-speed electrical machines: Technologies, trends, and developments," *IEEE Transactions on Industrial Electronics*, vol. 61, no. 6, pp. 2946–2959, 2014.
- [6] A. Chiba and T. Fukao, "Optimal design of rotor circuits in induction type bearingless motors," *IEEE Transactions on Magnetics*, vol. 34, no. 4, pp. 2108–2110, 1998.
- [7] A. Chiba and J. Asama, "Influence of rotor skew in induction type bearingless motor," *IEEE Transactions on Magnetics*, vol. 48, no. 11, pp. 4646–4649, 2012.
- [8] Y. Sun, J. Tang, and K. Shi, "Design of a bearingless outer rotor induction motor," *Energies*, vol. 10, no. 5, p. 705, 2017.
- [9] A. Chiba, T. Fukao, and M. A. Rahman, "Vibration suppression of a flexible shaft with a simplified bearingless induction motor drive," *IEEE Transactions on Industry Applications*, vol. 44, no. 3, pp. 745–752, May 2008.
- [10] V. F. Victor, J. Á. de Paiva, A. O. Salazar, and A. L. Maitelli, "Performance analysis of a neural flux observer for a bearingless induction machine with divided windings," in *2009 Brazilian Power Electronics Conference*. IEEE, 2009, pp. 498–504.
- [11] A. Sinervo and A. Arkkio, "Rotor radial position control and its effect on the total efficiency of a bearingless induction motor with a cage rotor," *Magnetics, IEEE Transactions on*, vol. 50, no. 4, pp. 1–9, April 2014.
- [12] J. Lu, Z. Yang, X. Sun, C. Bao, and X. Chen, "Direct levitation force control for a bearingless induction motor based on model prediction," *IEEE Access*, vol. 7, pp. 65 368–65 378, 2019.
- [13] X. Ye and Z. Yang, "Development of bearingless induction motors and key technologies," *IEEE Access*, vol. 7, pp. 121 055–121 066, 2019.
- [14] Z. Yang, Q. Ding, X. Sun, Q. Zhao, and J. Luo, "Analysis and optimisation of a bearingless induction motor's suspension force and unbalanced magnetic pulling force mathematical model," *IET Electric Power Applications*, 2020.
- [15] T. Tera, Y. Yamauchi, A. Chiba, T. Fukao, and M. A. Rahman, "Performances of bearingless and sensorless induction motor drive based on mutual inductances and rotor displacements estimation," *IEEE Transactions on Industrial Electronics*, vol. 53, no. 1, pp. 187–194, Feb 2006.
- [16] A. Chiba and J. A. Santisteban, "A pwm harmonics elimination method in simultaneous estimation of magnetic field and displacements in bearingless induction motors," *IEEE Transactions on Industry Applications*, vol. 48, no. 1, pp. 124–131, Jan 2012.
- [17] T. Wang, J. Huang, B. Lin, M. Kang, J. Chen, and W. Kong, "Eccentricity detection of a six-phase induction motor with hfi," *IET Electric Power Applications*, 2019.
- [18] K. Li, F. Ling, X. Sun, Y. Cai, D. Zhao, and Z. Yang, "Displacement sensorless control for bearingless induction motor drives based on the mras method," *International Journal of Applied Electromagnetics and Mechanics*, no. Preprint, pp. 1–19, 2020.
- [19] M. Kang, "Research on multiphase bearingless motors (in chinese)," Ph.D. dissertation, Zhejiang University, 2008.
- [20] J. Chen and E. L. Severson, "Design and modeling of the bearingless induction motor," in *2019 IEEE International Electric Machines and Drives Conference (IEMDC)*, May 2019, pp. 1–7.
- [21] ———, "Optimal design of the bearingless induction motor for industrial applications," in *2019 IEEE Energy Conversion Congress and Exposition (ECCE), September 2019, Baltimore, MD, USA.*, May 2019, pp. 1–7.
- [22] K. Campbell *et al.*, "High-speed induction motor with an integrated gearbox for propulsion," 2017.
- [23] C. Di, I. Petrov, and J. J. Pyrhönen, "Modeling and mitigation of rotor eddy-current losses in high-speed solid-rotor induction machines by a virtual permanent magnet harmonic machine," *IEEE Transactions on Magnetics*, vol. 54, no. 12, pp. 1–12, 2018.
- [24] N. Uzhevog, E. Kurvinen, J. Nerg, J. Pyrhönen, J. T. Sopanen, and S. Shirinskii, "Multidisciplinary design process of a 6-slot 2-pole high-speed permanent-magnet synchronous machine," *IEEE Transactions on Industrial Electronics*, vol. 63, no. 2, pp. 784–795, 2016.
- [25] A. Smirnov, N. Uzhevog, T. Sillanpää, J. Pyrhönen, and O. Pyrhönen, "High-speed electrical machine with active magnetic bearing system optimization," *IEEE Transactions on Industrial Electronics*, vol. 64, no. 12, pp. 9876–9885, 2017.
- [26] C. Di, I. Petrov, J. J. Pyrhönen, and X. Bao, "Unbalanced magnetic pull compensation with active magnetic bearings in a 2 mw high-speed induction machine by fem," *IEEE Transactions on Magnetics*, no. 99, pp. 1–13, 2018.
- [27] E. L. Severson, R. Nilssen, T. Undeland, and N. Mohan, "Design of dual purpose no-voltage combined windings for bearingless motors," *IEEE Transactions on Industry Applications*, vol. 53, no. 5, pp. 4368–4379, 2017.
- [28] H. Mitterhofer, B. Mrak, and W. Gruber, "Comparison of high-speed bearingless drive topologies with combined windings," *IEEE Transactions on Industry Applications*, vol. 51, no. 3, pp. 2116–2122, 2015.
- [29] D. Steinert, T. Nussbaumer, and J. W. Kolar, "Concept of a 150 krpm bearingless slotless disc drive with combined windings," in *Electric Machines & Drives Conference (IEMDC), 2013 IEEE International*. IEEE, 2013, pp. 311–318.
- [30] J. Huang, B. Li, H. Jiang, and M. Kang, "Analysis and control of multiphase permanent-magnet bearingless motor with a single set of half-coiled winding," *IEEE Transactions on Industrial Electronics*, vol. 61, no. 7, pp. 3137–3145, 2014.
- [31] G. Sala, G. Valente, A. Formentini, L. Papini, D. Gerada, P. Zanchetta, A. Tani, and C. Gerada, "Space vectors and pseudoinverse matrix methods for the radial force control in bearingless multisector permanent

- magnet machines," *IEEE Transactions on Industrial Electronics*, vol. 65, no. 9, pp. 6912–6922, 2018.
- [32] W. Khoo, "Bridge configured winding for polyphase self-bearing machines," *Magnetics, IEEE Trans on*, vol. 41, no. 4, pp. 1289–1295, 2005.
- [33] W. Khoo, K. Kalita, and S. Garvey, "Practical implementation of the bridge configured winding for producing controllable transverse forces in electrical machines," *IEEE Trans on Mag.*, vol. 47, no. 6, 2011.
- [34] E. Severson, S. Gандикота, and N. Mohan, "Practical implementation of dual-purpose no-voltage drives for bearingless motors," *IEEE Transactions on Industry Applications*, vol. 52, no. 2, pp. 1509–1518, March 2016.
- [35] R. Oishi, S. Horima, H. Sugimoto, and A. Chiba, "A novel parallel motor winding structure for bearingless motors," *Magnetics, IEEE Transactions on*, vol. 49, no. 5, pp. 2287–2290, 2013.
- [36] K. Raggl, T. Nussbaumer, and J. W. Kolar, "Comparison of separated and combined winding concepts for bearingless centrifugal pumps," *J. Power Electron.*, vol. 9, no. 2, pp. 243–258, 2009.
- [37] Y. Jiang and E. L. Severson, "Floating capacitor suspension inverter for parallel combined winding bearingless motors," *IEEE Transactions on Industry Applications*, vol. 56, no. 2, pp. 1518–1528, 2020.
- [38] R. S. Konwar, K. Kalita, A. Banerjee, and W. K. Khoo, "Electromagnetic analysis of a bridge configured winding cage induction machine using finite element method," *Progress In Electromagnetics Research B*, vol. 48, pp. 347–374, 2013.
- [39] T. Hiromi, T. Katou, A. Chiba, M. A. Rahman, and T. Fukao, "A novel magnetic suspension-force compensation in bearingless induction-motor drive with squirrel-cage rotor," *IEEE Transactions on Industry Applications*, vol. 43, no. 1, pp. 66–76, Jan 2007.
- [40] V. F. Victor, F. O. Quintaes, J. S. Lopes, L. d. S. Junior, A. S. Lock, and A. O. Salazar, "Analysis and study of a bearingless ac motor type divided winding, based on a conventional squirrel cage induction motor," *IEEE Transactions on Magnetics*, vol. 48, no. 11, pp. 3571–3574, 2012.
- [41] N. R. Hemenway, H. Gjeddal, and E. L. Severson, "Magnetic bearing technology for industrial bearingless motor systems," in *2019 IEEE Workshop on Electrical Machines Design, Control and Diagnosis (WEMDCD)*, 2019.
- [42] J. A. Santistebani, A. O. Salazar, and R. M. Stephan, "Modeling and analysis of a loaded bearingless machine," *EPE Journal*, vol. 10, no. 1, pp. 32–39, 2000.
- [43] A. Chiba, "Transfer characteristics of radial force of induction-type bearingless motors with four-pole rotor circuits," *5th ISMB*, 1996, 1996.
- [44] X. Ye, Z. Yang, and T. Zhang, "Modelling and performance analysis on a bearingless fixed-pole rotor induction motor," *IET Electric Power Applications*, vol. 13, no. 2, pp. 251–258, 2018.
- [45] J. M. S. Ferreira, M. Zucca, A. O. Salazar, and L. Donadio, "Analysis of a bearingless machine with divided windings," *IEEE Transactions on Magnetics*, vol. 41, no. 10, pp. 3931–3933, Oct 2005.
- [46] X. Liu, T. Shi, L. Ding, X. Shao, and G. Xu, "Analysis of radial force and torque for bearingless wound-rotor induction motor," in *2011 International Conference on Electrical Machines and Systems*, Aug 2011, pp. 1–5.
- [47] J. Pyrhonen, T. Jokinen, and V. Hrabovcová, *Design of rotating electrical machines*. Wiley. com, 2009.
- [48] D. Gerada, A. Mebarki, N. L. Brown, K. J. Bradley, and C. Gerada, "Design aspects of high-speed high-power-density laminated-rotor induction machines," *IEEE Transactions on Industrial Electronics*, vol. 58, no. 9, pp. 4039–4047, 2011.
- [49] Y. Kang and E. Severson, "Optimization framework for a large high speed bearingless permanent magnet motor," in *Sixteenth International Symposium on Magnetic Bearings*, 2018, pp. 1–10.
- [50] A. E. Fitzgerald, C. Kingsley, S. D. Umans, and B. James, *Electric machinery*. McGraw-Hill New York, 2003, vol. 5.
- [51] JMAG, "Transition to steady state in a short time," *JMAG White Papers*, 2017. [Online]. Available: <https://www.jmag-international.com/whitepapers/w-se-53/>
- [52] D. Lin, P. Zhou, N. Chen, C. Lu, and M. Christini, "Fast methods for reaching ac steady state in fe transient analysis," in *Electric Machines and Drives Conference (IEMDC), 2017 IEEE International*. IEEE, 2017, pp. 1–6.
- [53] A. Sternecki, O. Bíró, K. Preis, S. Rainer, and G. Ofner, "Numerical analysis of steady-state operation of three-phase induction machines by an approximate frequency domain technique," *e & i Elektrotechnik und Informationstechnik*, vol. 128, no. 3, pp. 81–85, 2011.
- [54] M. Rosu, P. Zhou, D. Lin, D. M. Ionel, M. Popescu, F. Blaabjerg, V. Rallabandi, and D. Staton, *Multiphysics Simulation by Design for Electrical Machines, Power Electronics and Drives*. John Wiley & Sons, 2017, vol. 66.
- [55] P. Ponomarev, "Elmer fem induction machine tutorial."
- [56] D. Meeker, "Finite element method magnetics," *FEMM*, 2010.
- [57] HBM, "MCS10-005-6C, Multi-Axis Sensor," Accessed April 1, 2020. Available: <https://www.hbm.com/en/5626/multi-axis-sensor-mcs10/>.
- [58] Y. Jiang, R. A. Torres, and E. L. Severson, "Current regulation in parallel combined winding bearingless motors," *IEEE Transactions on Industry Applications*, vol. 55, no. 5, pp. 4800–4810, 2019.
- [59] Q. Zhang and H. Li, "Moea/d: A multiobjective evolutionary algorithm based on decomposition," *IEEE Transactions on Evolutionary Computation*, vol. 11, no. 6, pp. 712–731, 2007.
- [60] R. Tanabe and H. Ishibuchi, "An analysis of control parameters of moea/d under two different optimization scenarios," *Applied Soft Computing*, vol. 70, pp. 22–40, 2018.
- [61] F. Biscani and D. Izzo, "esa/pagmo2: pagmo 2.10," Jan. 2019. [Online]. Available: <https://doi.org/10.5281/zenodo.2529931>
- [62] N. Bianchi, S. Bolognani, M. D. Pre, and G. Grezzani, "Design considerations for fractional-slot winding configurations of synchronous machines," *IEEE transactions on industry applications*, vol. 42, no. 4, pp. 997–1006, 2006.



Jiahao Chen (S'17-M'19) received the B.Sc. and Ph.D. degrees in electrical engineering from Zhejiang University, China, in 2014 and 2019, respectively. Since September 2018, he was a visiting scholar at the University of Wisconsin-Madison, USA for one year, where he was involved in bearingless motors. He is currently a post doctoral research fellow with Nanyang Technological University, Singapore. His research interests include electric machines, drives, and direct-drive technologies.



Yusuke Fujii (S'14-M'20) received the B.S., M.S., and Ph.D. degrees from the Department of Mechanical Engineering, Shizuoka University, Hamamatsu, Japan, in 2015, 2017, and 2020, respectively. Since September 2019, he was a visiting scholar at the University of Wisconsin-Madison for half a year, where he was involved in bearingless induction motor.

He is currently an assistant professor with the Department of Electrical and Electronic Engineering, Tokyo Institute of Technology, Japan. His research interests include bearingless motors, magnetic bearings and motor drive.

Dr. Fujii is a member of the Institute of Electrical and Electronics Engineers (IEEE), the Institute of Electrical Engineers of Japan (IEEJ), and the Japan Society of Mechanical Engineers (JSME).



Martin Willard Johnson received the B.Sc degree in mechanical engineering and mathematics in 2019 from the University of Wisconsin-Madison, USA. He is currently pursuing his M.S. degree in mechanical engineering at the University of Wisconsin-Madison, USA. His research interests include high speed motors, bearingless motors, and thermal/structural modeling of electric machines.



Ashad Farhan (S'20) received the B.E. degree in electrical engineering from Visvesvaraya Technological University (VTU), Belagavi, India in 2017. He is currently pursuing the M.S. degree in electrical engineering from the University of Wisconsin-Madison, USA. His interest is in the field of electric machine design, drives, with particular interest to the high-speed machines and bearingless motors.



Eric L. Severson (S'09-M'15) received the B.Sc. and PhD degrees in electrical engineering from the University of Minnesota, Minneapolis, USA in 2008 and 2015, respectively where he also worked as a post doctoral associate through 2016. He is currently an assistant professor at the University of Wisconsin-Madison.

Dr. Severson is an associate director of the Wisconsin Electric Machines and Power Electronics Consortium (WEMPEC) and fellow of the Grainger Institute for Engineering. His research interests include design and control of electric machines and power electronics, with focus areas in magnetic bearings, bearingless motors, flywheel energy storage, and off-highway vehicle electrification.

Dr. Severson is a recipient of the USA National Science Foundation CAREER Award in 2020, the Department of Defense NDSEG fellowship in 2009, and the National Science Foundation Graduate Research Fellowship in 2009.